Commun. Comput. Phys.
doi: 10.4208/cicp.120210.240511a

Vol. **11**, No. 5, pp. 1643-1672
May 2012

A Well-Posed and Discretely Stable Perfectly Matched Layer for Elastic Wave Equations in Second Order Formulation

Kenneth Duru* and Gunilla Kreiss

Division of Scientific Computing, Department of Information Technology, Uppsala University, Box 337, SE-751 05 Uppsala, Sweden.

Received 12 February 2010; Accepted (in revised version) 24 May 2011

Communicated by Jan S. Hesthaven

Available online 12 January 2012

Abstract. We present a well-posed and discretely stable perfectly matched layer for the anisotropic (and isotropic) elastic wave equations without first re-writing the governing equations as a first order system. The new model is derived by the complex coordinate stretching technique. Using standard perturbation methods we show that complex frequency shift together with a chosen real scaling factor ensures the decay of eigen-modes for all relevant frequencies. To buttress the stability properties and the robustness of the proposed model, numerical experiments are presented for anisotropic elastic wave equations. The model is approximated with a stable node-centered finite difference scheme that is second order accurate both in time and space.

AMS subject classifications: 35B35, 35L05, 35L15, 37C75

Key words: Perfectly matched layer, well-posedness, stability, hyperbolicity, elastic waves.

1 Introduction

Perfectly matched layers (PML) have since the introduction [3], emerged as a standard non-reflecting boundary closure for many wave propagation problems. The basic properties of a PML can be found in [6]. In this paper we consider linear, anisotropic elastodynamics in two space dimensions. Equations describing the dynamics are usually derived via Newton's law, which connects acceleration and force, and yields a second order system (in both time and space) for the displacements. The system is hyperbolic, and by introducing suitable variables the model can be rewritten as a hyperbolic first

*Corresponding author. *Email addresses:* kenneth.duru@it.uu.se (K. Duru), gunilla.kreiss@it.uu.se (G. Kreiss)

order system. PMLs for elasto-dynamics are usually derived from the first order formulation [4, 5, 23]. This is also the case for other hyperbolic systems that naturally come in second order formulation, like the standard wave equation.

However, there are several advantages with using the second order formulation. The first order formulation requires more variables, and it introduces a new wave with zero wave speed. Also, in many cases a straightforward discretization of the first order formulation introduces high frequency spurious modes. In this paper we construct a PML for the second order equations of linear, anisotropic elasto-dynamics in two space dimensions without first rewriting the equations as a first order system. By construction the PML is perfectly matched, but there is no guarantee that all solutions decay with time. The analysis of temporal stability is therefore a main topic of research. In [4], the geometric stability condition was formulated, and found to be a necessary condition for stability of the split field PML. In [5], it was proved to be necessary also for stability of a modal PML, even though the complex frequency shift had a stabilizing effect.

The aim of this paper is to construct efficient layers based on the second order equations, for all materials, and also those violating the geometric stability condition. The PML equations are derived using a complex coordinate stretching technique, [6, 17]. We include a grid stretching parameter and a complex frequency shift. One advantage of this approach is that we can choose auxiliary variables so that the resulting system is strongly hyperbolic.

In computations using standard second order central finite differences, our PML behaves dramatically better than the corresponding first order PMLs, for materials where the geometric stability condition is violated. In many cases no growth is seen in the computation even at very late times. A large part of the paper is dedicated to understanding why our PML behaves in this stable way, and how the stable behavior can be enhanced.

We start by applying a standard perturbation analysis to our PML at constant coefficients. The result is that our PML suffers from the same high frequency instability as the above mentioned first order PMLs for the geometric stability violating materials. From the analysis we know that the instability appears only at sufficiently high spatial frequencies. If these frequencies are not well resolved, the discrete behavior may be completely different. A straight forward computation of the temporal eigenvalues corresponding to the discrete spatial operator in a constant coefficient setting shows that if unstable modes are not well resolved, they are in fact stable in the discrete setting. We have investigated how the grid stretching parameter can be used to enhance this effect.

A second reason is the stabilizing effect of corner regions. When the layers are used as boundary closures completely surrounding a domain there are usually corner regions. We use the same perturbation technique as above applied to a constant coefficient corner problem, and find that our PML is significantly more stable in the corner region. In computations we have observed that the bulk of an unstable mode typically is localized to part of the layer and propagates tangentially while the amplitude grows. Eventually the bulk of the unstable mode moves into a corner region and is damped.

The paper is organized as follows. In Section 2 we introduce the elastic wave equa-

tion, the materials treated in the paper, and their corresponding dispersion relations. A brief review of existing layers and there properties are given, followed by a derivation of our layer. The basic mathematical properties such as perfect matching, hyperbolicity and wellposedness are discussed. Section 3 is devoted to stability analysis. In Section 4 we present numerical calculations both as illustration of our theoretical results, and to further explore the properties of our layer. We close Section 4 by investigating the efficiency of the layer. We present computations where we show that it is possible to chose parameters related to the spatial step size yielding reflections from the layer that decay as $h \to 0$. In Section 5 a brief conclusion is offered.

2 Elastic waves and damping layers

In this section, the second order equations of linear elastodynamics (in orthotropic media) in two space dimensions will be stated and we will derive the PML model using a complex coordinate stretching technique.

2.1 Elastic waves

Using Einstein's convention of summation and neglecting body forces, the equation of continuum can be written

$$\rho \frac{\partial^2 u_i}{\partial t^2} = \frac{\partial \sigma_{i,j}}{\partial x_j}, \qquad i,j = 1,2. \tag{2.1}$$

Here ρ is the density and u_1, u_2 are the displacement, $\sigma_{i,j}$ is the stress tensor, which is related to the tensor of deformation

$$\epsilon_{i,j}(u) = \frac{1}{2}\Big(\frac{\partial u_i}{\partial x_j} + \frac{\partial u_j}{\partial x_i}\Big).$$

By Hooke's law

$$\sigma_{i,j} = C_{ijkl}\epsilon_{kl}. \tag{2.2}$$

The fourth-order tensor C of elastic coefficients satisfies the classical symmetries

$$C_{ijkl} = C_{jikl} = C_{klij}.$$

It is also positive definite,

$$C_{ijkl}\psi_{ij}\psi_{kl} \geq \|\psi\|^2 = \alpha\psi_{ij}\psi_{ij},$$

for all symmetric tensor ψ_{ij}, see [25]. The symmetry of C allows us to simplify the equations by using the scheme

$$C_{ijkl} = c_{p(i,j),p(k,l)},$$

where $p(i,j)=i$, if $i=j$, $p(i,j)=i+j$, if $i\neq j$.

In an orthotropic medium whose principal axes coincides with the (x,y) axes, we have $c_{13}=c_{23}=0$, hence

$$C=\begin{pmatrix} c_{11} & c_{12} & 0 \\ c_{21} & c_{22} & 0 \\ 0 & 0 & c_{33} \end{pmatrix}.$$

Now Eq. (2.1) can be formally written as

$$\mathbf{u}_{tt}=A_1\mathbf{u}_{xx}+A_2\mathbf{u}_{yy}+A_3\mathbf{u}_{xy}, \tag{2.3}$$

where

$$\mathbf{u}=[u_1,u_2]^T, \quad A_1=\begin{pmatrix} a & 0 \\ 0 & c \end{pmatrix}, \quad A_2=\begin{pmatrix} c & 0 \\ 0 & b \end{pmatrix}, \quad A_3=\begin{pmatrix} 0 & d \\ d & 0 \end{pmatrix}.$$

Here $a=c_{11}$, $b=c_{22}$, $c=c_{33}$, $d=c_{33}+c_{21}$. For convenience we have also assumed $\rho=1$. It is easy to show that (2.3) is strongly hyperbolic and strongly well-posed.

2.2 Plane waves and slowness diagrams

In order to understand the wave propagation properties of the model (2.3) it is useful to consider wave-like solutions

$$\mathbf{u}=\mathbf{u}_0 e^{st-ik_x x-ik_y y}, \quad \mathbf{u}_0\in\mathbb{R}^n, \qquad k_x,k_y,x,y\in\mathbb{R}, \quad 0\leq t. \tag{2.4}$$

In Eq. (2.4), $(k_x,k_y)\in\mathbb{R}^2$ is the wave vector, and $\mathbf{u}_0$ is a vector of constant amplitude called the polarization vector. By inserting (2.4) in (2.3) we have a solvability condition (2.5), often called the dispersion relation

$$F_0(s,k_x,k_y)\equiv det(s^2 I+\Psi(k_x,k_y))=0, \qquad \Psi(k_x,k_y)=A_1k_x^2+A_2k_y^2+A_3k_xk_y. \tag{2.5}$$

The polarization vector $\mathbf{u}_0$ is the eigenvector of $\Psi(k_x,k_y)$, with associated eigenvalue $-s^2$. By evaluating (2.5) for (2.3) we have

$$s^4+\big((a+c)k_x^2+(b+c)k_y^2\big)s^2+ack_x^4+bck_y^4+(ab+c^2-d^2)k_x^2k_y^2=0. \tag{2.6}$$

It should be noted that the polynomial (2.6) has four purely imaginary roots, corresponding to the quasi-P and quasi-S waves. We will refer to these modes as the physical modes.

If we write $s=i\omega(k_x,k_y)$, where $\omega\in\mathbb{R}$ is called the temporal frequency, we can also

introduce

$$K=\Big(\frac{k_x}{|k|},\frac{k_y}{|k|}\Big), \qquad \text{the normalized propagation direction,} \tag{2.7a}$$

$$V_p=\Big(\frac{\omega}{k_x},\frac{\omega}{k_y}\Big), \qquad \text{the phase velocity,} \tag{2.7b}$$

$$S=\Big(\frac{k_x}{\omega},\frac{k_y}{\omega}\Big), \qquad \text{the slowness vector,} \tag{2.7c}$$

$$V_g=\nabla_k\omega(k_x,k_y), \qquad \text{the group velocity,} \tag{2.7d}$$

and

$$|k|=\sqrt{k_x^2+k_y^2}. \tag{2.7e}$$

By inspection (2.6) is homogeneous in ω, k_x,k_y, we can rewrite (2.6) as

$$F_0(i,S)=0. \tag{2.8}$$

The wave propagation properties of a certain medium can be described by plotting the slowness diagrams defined by points in the S-plane satisfying (2.8). If we further assume $c_{11}\neq c_{33}$ and $c_{22}\neq c_{33}$, the group velocity can be expressed as

$$V_g=\nabla_k\omega(k_x,k_y)=-\Big(\frac{\partial F_0(i\omega,k_x,k_y)}{\partial\omega}\Big)^{-1}\nabla_k F_0(i\omega,k_x,k_y). \tag{2.9}$$

That is, the group velocity is normal to the slowness curve. In [4] geometric stability conditions are introduced. We have

Definition 2.1. [Geometric stability condition]

1. The geometric stability condition in the x-direction is $S_x\times(V_g)_x\geq 0$, for all points on the slowness curve.
2. The geometric stability condition in the y-direction is $S_y\times(V_g)_y\geq 0$, for all points on the slowness curve.

Here $V_g=((V_g)_x,(V_g)_y)$ and $S=(S_x,S_y)$.

By Theorem 2 in [4] the geometric stability condition in the $x(y)$-direction is necessary for stability of the vertical (horizontal) PML. The material parameters we will consider in this paper are presented in Table 1. The anisotropic material MA1 with the slowness diagram Fig. 2(a) severely violates the geometric stability conditions in both x- and y-directions, and is the same as material III in [4,5]. The anisotropic material MA2 (Apatite) marginally violates the geometric stability condition in both x- and y-direction, see Fig. 2(b), and has been studied in [16]. The material MA3 violates the geometric stability condition only in the y-direction, see Fig. 2(c). The anisotropic material MA4 (Zinc crystal) violates the stability condition in the x-direction, see Fig. 2(d), and has also been

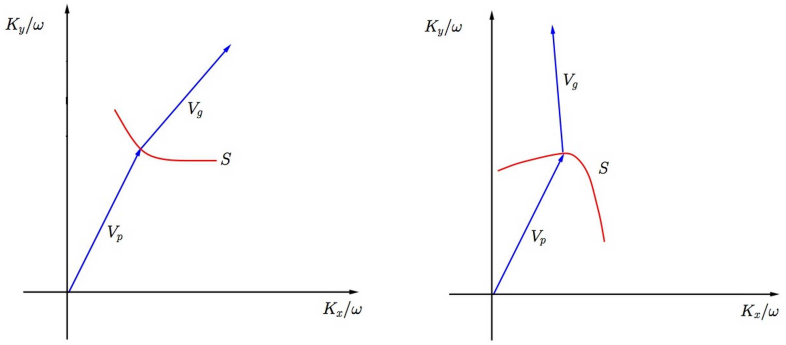

(a) Stable. (b) Unstable.

Figure 1: Geometric stability condition.

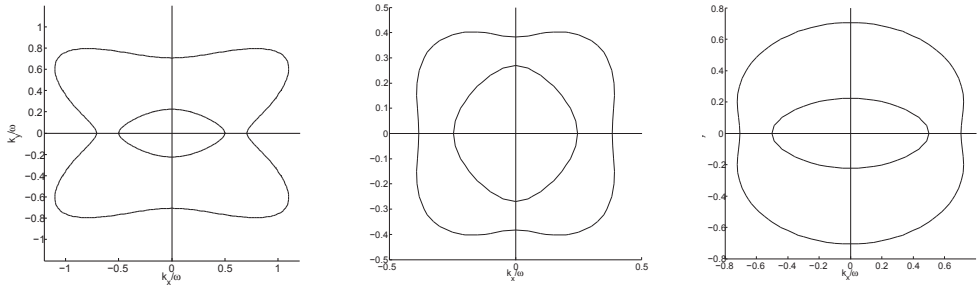

(a) [MA1]. (b) [MA2]. (c) [MA3].

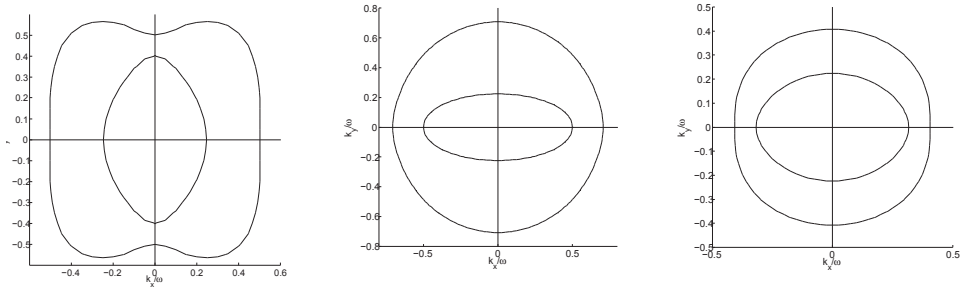

(d) [MA4]. (e) [MB]. (f) [MC].

Figure 2: Slowness diagrams.

studied in [16]. For the materials MA1 and MA2, the classical PML in both x- and y-directions will be unstable, while the y-dependent PML for material MA3 will be unstable. Since material MA4 violates the geometric stability condition only in the x-direction, the x-dependent PML for material MA4 will be unstable. The anisotropic material MB is the same as Material I in [5] and does not violate the stability condition, the classical PML for the material MB is expected to be stable. Though material MC (same as Material IV in [5]) does not violate the geometric stability condition, it has a generic weak instability as demonstrated in [4].

Table 1: Elastic coefficients of the orthotropic materials.

Material	Elastic Coefficients			
	c_{11}	c_{22}	c_{33}	c_{12}
MA1	4.00	20.00	2.00	7.50
MA2	16.70	14.00	6.63	6.60
MA3	4.00	20.00	2.00	4.90
MA4	16.50	6.20	3.96	5.00
MB	4.00	20.00	2.00	3.80
MC	10.00	20.00	6.00	2.50

2.3 Damping layers for elastic wave equations

Several damping layers exist for the elastic wave equations, [4,5,8,23]. Many of these layers are only weakly hyperbolic and weakly well-posed. In many cases the existing layers also support exponentially growing solution. This shortcoming, for the classical PML for elastic waves as reported in [4], was in part corrected in [5] by adding the complex frequency shift in a modal PML for the first order formulation. For materials that violate the geometric stability condition, the construction of a stable and efficient absorbing layer has remained a challenge.

In a very recent work [16], the multi-axial perfectly matched layer (M-PML) was proposed. Their model is based on a damping profile that varies in more than one direction. This approach may give a stable model for some materials but it generates non-trivial reflections from the interface of the layer and the computational domain and therefore is not perfectly matched. In numerical experiments we have also observed that long-time solutions of the M-PML model may exhibit growth as the solutions reach quiescent state.

2.4 Our perfectly matched layer

In this section, we will derive PML equations using the complex coordinate stretching technique, see [6, 17]. The idea is to introduce new coordinates defined by special complex metrics. The PML can be viewed as the complex change of variables in the Fourier transformed wave equation. We begin with a Fourier transformation in time,

$$\mathbf{u}(x,y,t)=\int_{-\infty}^{\infty}\hat{\mathbf{u}}(x,y,\omega)e^{i\omega t}d\omega, \qquad -\omega^2\hat{\mathbf{u}}=A_1\hat{\mathbf{u}}_{xx}+A_2\hat{\mathbf{u}}_{yy}+A_3\hat{\mathbf{u}}_{xy}. \tag{2.10}$$

To include PML in both x-direction and y-direction we introduce the complex metrics,

$$s_1=\alpha_1(x)\Big(1+\frac{\sigma_1(x)}{\eta+i\omega}\Big), \qquad s_2=\alpha_2(y)\Big(1+\frac{\sigma_2(y)}{\eta+i\omega}\Big),$$

yielding

$$-\omega^2\hat{\mathbf{u}}=A_1\frac{1}{s_1}\Big(\frac{1}{s_1}\hat{\mathbf{u}}_x\Big)_x+A_2\frac{1}{s_2}\Big(\frac{1}{s_2}\hat{\mathbf{u}}_y\Big)_y+A_3\frac{1}{s_1}\frac{1}{s_2}\hat{\mathbf{u}}_{xy}. \tag{2.11}$$

Here, $\eta \geq 0$ is the complex frequency shift, α_1, $\alpha_2 > 0$, are grid compression (or stretching) functions and $\sigma_1, \sigma_2 \geq 0$ are the damping functions. The functions α_1, α_2, σ_1, σ_2 are required to be smooth. A_1, A_2, A_3 are elastic coefficients defined just after (2.3).

By choosing the auxiliary variables, and inverting the Fourier transform we have the full PML formulation

$$\begin{aligned}\mathbf{u}_{tt} = &\frac{1}{\alpha_1}A_1\Big(\frac{1}{\alpha_1}\mathbf{u}_x\Big)_x + \frac{1}{\alpha_2}A_2\Big(\frac{1}{\alpha_2}\mathbf{u}_y\Big)_y + \frac{1}{\alpha_1\alpha_2}A_3\mathbf{u}_{xy}\\ &-\frac{1}{\alpha_1}A_1\Big(\frac{\sigma_1}{\alpha_2}\mathbf{v}-\frac{\sigma_2}{\alpha_1}\mathbf{w}\Big)_x + \frac{1}{\alpha_2}A_2\Big(\frac{\sigma_1}{\alpha_2}\mathbf{q}-\frac{\sigma_2}{\alpha_1}\mathbf{p}\Big)_y - (\sigma_1+\sigma_2)\mathbf{u}_t\\ &+(\sigma_1+\sigma_2)\eta(\mathbf{u}-\mathbf{r}) - \sigma_1\sigma_2\big((\mathbf{u}-\mathbf{r})-(\mathbf{r}-\mathbf{z})\big), \qquad (2.12a)\end{aligned}$$

$$\mathbf{v}_t = \frac{\alpha_2}{\alpha_1}u_x + \frac{\alpha_2}{\alpha_1}\sigma_2\mathbf{w} - (\sigma_1+\eta)\mathbf{v}, \qquad \mathbf{w}_t = \mathbf{u}_x - \eta\mathbf{w}, \qquad (2.12b)$$

$$\mathbf{p}_t = \frac{\alpha_1}{\alpha_2}\mathbf{u}_y + \frac{\alpha_1}{\alpha_2}\sigma_1\mathbf{q} - (\sigma_2+\eta)\mathbf{p}, \qquad \mathbf{q}_t = \mathbf{u}_y - \eta\mathbf{q}, \qquad (2.12c)$$

$$\mathbf{r}_t = \eta(\mathbf{u}-\mathbf{r}), \qquad \mathbf{z}_t = \eta(\mathbf{r}-\mathbf{z}). \qquad (2.12d)$$

In order to investigate some of the mathematical properties of the PML model (2.12) we will consider the vertical layer (parallel to the y-axis). We set $\sigma_2 = 0$, $\alpha_2 = 1$ in (2.12) and obtain the reduced system

$$\mathbf{u}_{tt} = \frac{1}{\alpha_1}A_1\Big(\frac{1}{\alpha_1}\mathbf{u}_x\Big)_x + A_2\mathbf{u}_{yy} + \frac{1}{\alpha_1}A_3\mathbf{u}_{xy} - \frac{1}{\alpha_1}A_1(\sigma_1\mathbf{v})_x + A_2(\sigma_1\mathbf{w})_y - \sigma_1\mathbf{u}_t + \eta\sigma_1(\mathbf{u}-\mathbf{r}), \qquad (2.13a)$$

$$\mathbf{v}_t = \frac{1}{\alpha_1}\mathbf{u}_x - (\sigma_1+\eta)\mathbf{v}, \qquad \mathbf{w}_t = \mathbf{u}_y - \eta\mathbf{w}, \qquad \mathbf{r}_t = \eta(\mathbf{u}-\mathbf{r}). \qquad (2.13b)$$

By construction the model (2.13) is perfectly matched if $\sigma_1 = 0$ and $\alpha_1 = 1$ at the interface between the physical domain and the layer.

2.5 Hyperbolicity and well-posedness

For convenience we shall rewrite (2.13) as a first order system in time and space. Without loss of generality we consider $\eta = 0$, $\alpha_1 = 1$, introduce the auxiliary variables,

$$U_1 = \mathbf{u}, \quad U_2 = \mathbf{v}, \quad U_3 = \mathbf{w}, \quad U_4 = \int_0^t (\mathbf{u}_y + \sigma_1\mathbf{w})d\tau,$$

and we have

$$U_t = B_xU_x + B_yU_y + \sigma_1 CU. \qquad (2.14)$$

Here

$$B_x = \begin{pmatrix}\mathbf{0} & A_1 & A_3 & \mathbf{0}\\ \mathbf{I} & \mathbf{0} & \mathbf{0} & \mathbf{0}\\ \mathbf{0} & \mathbf{0} & \mathbf{0} & \mathbf{0}\\ \mathbf{0} & \mathbf{0} & \mathbf{0} & \mathbf{0}\end{pmatrix}, \qquad B_y = \begin{pmatrix}\mathbf{0} & \mathbf{0} & \mathbf{0} & A_2\\ \mathbf{0} & \mathbf{0} & \mathbf{0} & \mathbf{0}\\ \mathbf{I} & \mathbf{0} & \mathbf{0} & \mathbf{0}\\ \mathbf{I} & \mathbf{0} & \mathbf{0} & \mathbf{0}\end{pmatrix}, \qquad C = \begin{pmatrix}\mathbf{-I} & \mathbf{0} & \mathbf{0} & \mathbf{0}\\ \mathbf{0} & \mathbf{-I} & \mathbf{0} & \mathbf{0}\\ \mathbf{0} & \mathbf{0} & \mathbf{0} & \mathbf{0}\\ \mathbf{0} & \mathbf{0} & \mathbf{I} & \mathbf{0}\end{pmatrix},$$

where $\mathbf{0}$ is a 2×2 null matrix and $\mathbf{I}$ is a 2×2 identity matrix.

It is easy to show that $\forall S=(S_x,S_y)\in\mathbb{R}^2$ normalized to satisfy (2.8), the matrix $\hat{B}=S_xB_x+S_yB_y$ has real eigenvalues and a complete system of eigen-vectors. It follows that the PML model (2.13) is strongly hyperbolic, thus strongly well-posed, see [12]. However, because of the lower order term $\sigma_1 CU$ the system (2.13) may have solutions that grow in time. It is important to note that strong hyperbolicity guarantees the well-posedness of partial differential equations under all lower order perturbations. The first order split-field or modal PML formulations for the elastic wave equation are only weakly hyperbolic and lack this important property [4,5]. Including $\eta\neq 0$, will correspond to adding more zeros to the columns and rows of the matrices B_x, B_y and the corresponding principal part is strongly hyperbolic.

3 Stability analysis

In this section we will explore the stability properties of the proposed layer. The perfectly matched layer is indeed a variable coefficient problem, but the mathematical tools readily available only allows for the analysis of the corresponding constant coefficient problem. Here we use standard perturbation techniques similar to the methods used in [4,5,16], to analyze the corresponding constant coefficient Cauchy problem.

3.1 Stability of the standard PML

To begin with, consider the model (2.13). We will show that at constant coefficients our layer suffers from the so called geometric (high frequency) instability. By introducing the modal ansatz $\mathbf{W}=\mathbf{W}_0e^{st-ik_xx-ik_yy}$, where (k_x,k_y) is the wave vector, and $\mathbf{W}=[\mathbf{u},\mathbf{v},\mathbf{w},\mathbf{r}]^T$, we get the characteristic polynomial

$$F\Big(s,\frac{k_x}{\alpha_1},k_y,\sigma_1,\eta\Big)\equiv(s+\eta)^2F_0\Big((s+\sigma_1+\eta)s,\frac{(s+\eta)k_x}{\alpha_1},(s+\sigma_1+\eta)k_y\Big)=0. \tag{3.1}$$

F_0 is defined in (2.5). The stability of the PML model (2.13) is characterized by the roots s of the polynomial (3.1). In order to determine whether (2.13) is stable or unstable we only need to know the sign of the real part of s, $\Re s$, as we introduce damping.

First, we will characterize the roots of the undamped system. By setting $\sigma_1=0$ in (3.1) we have

$$F\Big(s,\frac{k_x}{\alpha_1},k_y,0,\eta\Big)=(s+\eta)^6F_0\Big(s,\frac{k_x}{\alpha_1},k_y\Big). \tag{3.2}$$

Clearly (3.2) has 10 roots, 4 of which are the purely imaginary roots of (2.6) and correspond to the physical (quasi-P and quasi-S) modes. The remaining 6 roots are real and non-positive

$$s_m=\{-\eta\},\qquad m=5,6,\cdots,10. \tag{3.3}$$

We call the corresponding modes non-physical. Since the roots depend continuously on the coefficients, it is apparent that at intermediate frequencies and with small enough damping the roots s of the non-physical modes will remain in the left half of the complex plane. Thus we have

Lemma 3.1. *At intermediate frequencies, if $\eta>0$ and $\alpha_1>0$, the non-physical modes s are stable for all sufficiently small damping $\sigma_1\geq 0$.*

At high frequencies a more refined analysis is needed.

Lemma 3.2. *For any $\alpha_1>0$ and for sufficiently small damping $\sigma_1\geq 0$, the parameter $\eta>0$ will stabilize the non-physical modes at high frequencies.*

Proof. We introduce the normalized variables,

$$\lambda=\frac{s}{|k|},\quad k_1=\frac{k_x}{|k|},\quad k_2=\frac{k_y}{|k|},\quad \epsilon=\frac{\sigma_1}{|k|},\quad \gamma=\frac{\eta}{|k|},\quad |k|=\sqrt{k_x^2+k_y^2}, \tag{3.4}$$

in (3.1) and we have

$$(\lambda+\gamma)^2F_0\Big((\lambda+\epsilon+\gamma)\lambda,\frac{(\lambda+\gamma)k_1}{\alpha_1},(\lambda+\epsilon+\gamma)k_2\Big)=0. \tag{3.5}$$

Remark 3.1. It is possible to normalize by $|k|=\sqrt{k_x^2/\alpha_1^2+k_y^2}$ such that (3.5) is independent of α_1. We instead interpret α_1 as a rescaling of the elastic coefficients and consider the normalization as given by (3.4).

The non-physical modes are continuous functions of ϵ and therefore can be expanded by a *Puiseux* series, see [24],

$$\lambda\Big(\frac{k_1}{\alpha_1},k_2,\epsilon\Big)=-\gamma+\Upsilon^\gamma\Big(\frac{k_1}{\alpha_1},k_2\Big)\epsilon^r+o(\epsilon^r),\quad r\in\mathbb{Q}^+. \tag{3.6}$$

If $r\geq 1$, then we know that the perturbed root λ will have a negative real part for sufficiently high frequencies and $\epsilon/\gamma\ll 1$, hence the non-physical modes are stable. Let us assume that there exists a solution such that $0<r<1$ and $\Upsilon^\gamma\neq 0$. By inserting the expression (3.6) in (3.5) we have

$$\begin{aligned}
&\Big(\Upsilon^\gamma\Big(\frac{k_1}{\alpha_1},k_2\Big)\epsilon^r\Big)^6F_0\Big(-\gamma+\mathcal{O}(\epsilon^r),\frac{k_1}{\alpha_1}+o(1),k_2+o(1)\Big)=0,\\
\Longrightarrow&\Big(\Upsilon^\gamma\Big(\frac{k_1}{\alpha_1},k_2\Big)\epsilon^r\Big)^6F_0\Big(-\gamma,\frac{k_1}{\alpha_1},k_2\Big)+o(1)=0,\\
\Longrightarrow&\Big(\Upsilon^\gamma\Big(\frac{k_1}{\alpha_1},k_2\Big)\epsilon^r\Big)^6F_0\Big(-\gamma,\frac{k_1}{\alpha_1},k_2\Big)=0.
\end{aligned}$$

Since $F_0(-\gamma,k_1/\alpha_1,k_2)\neq 0$ for all $\gamma\in\mathbb{R}^+$, it follows that $\Upsilon^\gamma=0$, which is a contradiction. We must have $r\geq 1$ and the lemma is shown. □

We note that the proof of Lemma 3.2 is analogous to the proofs of Lemma 7 in [5] and Theorem 1 in [4].

We see that if $\eta>0$ the instability in the standard PML at constant coefficients can not come from the non-physical modes. In order to understand the stability of the physical modes we perform the high frequency stability analysis due to [4]. To begin with, we consider $\alpha_1=1$. The physical modes are simple (distinct), therefore can be expanded in the powers of ϵ,

$$\lambda=\lambda_0+\epsilon\lambda_\epsilon+\mathcal{O}(\epsilon^2). \tag{3.7}$$

Here λ_0 is a purely imaginary root of $F_0(\lambda,k_1,k_2)$. At sufficiently high frequencies, $\epsilon\ll 1$, we can ignore higher order terms in ϵ, and the sign of the real part of λ_ϵ determines the stability of (2.13).

Consider

$$F_0\Big(\lambda,\Big(1+\frac{\epsilon}{\lambda+\gamma}\Big)^{-1}k_1,k_2\Big)=0,$$

and expand in the powers of ϵ, and we have

$$F_0(\lambda_0,k_1,k_2)+\epsilon\Big(\lambda_\epsilon\frac{\partial F_0}{\partial\lambda}-\frac{k_1}{\lambda_0+\gamma}\frac{\partial F_0}{\partial k_1}\Big)+\mathcal{O}(\epsilon^2)=0.$$

By ignoring higher order terms and using that λ_0, $\partial F_0/\partial\lambda$ are purely imaginary, we have

$$\Re\lambda_\epsilon=-\frac{|\lambda_0|^2}{\gamma^2+|\lambda_0|^2}\frac{k_1}{\lambda_0}\Big(-\frac{\partial F_0}{\partial\lambda}\Big)^{-1}\frac{\partial F_0}{\partial k_1}. \tag{3.8}$$

We see that a physical mode will be unstable if

$$\frac{k_1}{\lambda_0}\Big(-\frac{\partial F_0}{\partial\lambda}\Big)^{-1}\frac{\partial F_0}{\partial k_1}<0. \tag{3.9}$$

Remember if we replace $s=i\omega$, where ω is the temporal frequency we have

$$\Re\lambda_\epsilon=-\frac{|\omega|^2}{\gamma^2+|\omega|^2}\frac{k_x}{\omega}\Big(-\frac{\partial F_0}{\partial\omega}\Big)^{-1}\frac{\partial F_0}{\partial k_x}=-\frac{|\omega|^2}{\gamma^2+|\omega|^2}S_x\times(V_g)_x. \tag{3.10}$$

Therefore, the relation (3.9) is equivalent to the so called geometric stability condition in the x-direction. By Definition 2.1 we have proved the following

Lemma 3.3. *Consider $\alpha_1=1$ and $\sigma_1>0$. If the geometric stability condition in the x-direction is violated there are unstable physical modes at sufficiently high frequencies.*

By computing the roots of (3.5) for a set of frequencies we also observed that increasing the complex frequency shift η for a fixed σ_1 can move most of the unstable physical modes into the stable complex plane. However if $\eta\gg\sigma_1$ the whole spectrum moves towards the imaginary axis, indicating weak damping.

3.2 Grid compression

Here we investigate the effect of the grid compression parameter α_1 on the physical modes. Looking again at the slowness diagrams in Fig. 2, we see that if the geometric stability condition is violated, the modes on the slowness curve violating the geometric stability condition in the x-direction satisfy the relation

$$\frac{|S_x|}{|S_y|} \leq \kappa, \tag{3.11}$$

for some $\kappa > 0$. For any anisotropic elastic material, the instability parameter κ can be determined precisely from the slowness diagrams.

Lemma 3.4. *Assume there exists a $\kappa > 0$ such that the geometric stability condition in the x-direction is violated for modes satisfying* (3.11). *Given σ_1, $k_0 > 0$ there exists $\alpha_0 > 0$ such that for all $0 < \alpha_1 \leq \alpha_0$ and all $\eta \geq 0$, the physical modes with the normalized frequencies (k_1, k_2) in the range $k_0 < |k_1| \leq 1$, $0 \leq |k_2| \leq 1$, are stable at sufficiently high frequencies.*

Proof. We repeat the analysis above with $0 < \alpha_1 < 1$, arriving at

$$\Re\lambda_\epsilon = -\frac{|\lambda_0|^2}{\gamma^2 + |\lambda_0|^2} \frac{k_1}{\alpha_1 \lambda_0} \Big(-\frac{\partial F_0}{\partial \lambda} \Big)^{-1} \frac{\partial F_0}{\partial k_1}, \tag{3.12}$$

where $\lambda_0(k_1/\alpha_1, k_2)$ is a root of $F_0(\lambda, k_1/\alpha_1, k_2) = 0$. Note that

$$\frac{\partial F_0}{\partial \lambda}, \quad \frac{\partial F_0}{\partial k_1},$$

are evaluated at $\lambda_0(k_1/\alpha_1, k_2)$, k_1/α_1, k_2. If $\alpha_1 = k_0/\kappa$ then for all k_2 and $|k_1| \geq k_0$, the expression (3.12) will be evaluated at $\tilde{k}_1 = k_1/\alpha_1$, $\tilde{k}_2 = k_2$ corresponding to a point on the slowness curve where

$$\frac{|\tilde{k}_1|}{|\tilde{k}_2|} = \frac{|S_x|}{|S_y|} = \frac{k_1}{\alpha_1 k_2} \geq \frac{k_0}{\alpha_1 k_2} \geq \frac{\kappa}{k_2} \geq \kappa.$$

Thus $\Re\lambda_\epsilon < 0$ and all physical modes with the normalized frequencies (k_1, k_2) in the range $k_0 < |k_1| \leq 1$, $0 \leq |k_2| \leq 1$, are stable. □

A direct consequence of Lemmas 3.2 and 3.4 is the corollary

Corollary 3.1. *Assume α_1, η satisfy the conditions in Lemmas* 3.2 *and* 3.4. *For sufficiently high frequencies $|k|$ the constant coefficient PML model* (2.13) *is asymptotically stable for all frequencies, $|k_0| < |k_1| \leq 1$, $0 \leq |k_2| \leq 1$.*

In order to highlight the above result, we perform the semi-discrete analysis below and consider two materials Apatite and Zinc crystal violating the geometric stability condition, see Figs. 2(b) and 2(d).

3.3 Semi-discrete analysis

In a discrete setting a finite number of grid points are used, and only certain frequencies can be represented. For a given discretization instability or stability in the continuous model can be strengthened or weakened. We expect a layer to be unstable, at least if modes violating the stability condition can be represented and are well resolved. In this subsection we demonstrate that un-resolved modes are in fact more stable than predicted by the continuous analysis. We also demonstrate that for a chosen discretization, the grid compression parameter α_1 can be chosen such that the discrete PML is stable.

Consider 2π-periodic problem (in both space directions), with constant coefficients, discretized by $N=2M+1$ equally spaced grid points in each spatial direction. The spatial step is $h=2\pi/N$, and modes with wave numbers k_x, $k_y=0,\pm1,\pm2,\cdots,\pm M$ can be represented. Replacing derivatives with standard second order central differences in the right hand side of (2.13), we have the semi-discrete problem

$$\mathbf{u}_{tt}+\sigma_1\mathbf{u}_t=L_h(\mathbf{u})+F_h(u,\Theta,\sigma_1,\eta),\qquad \Theta_t=J_h(\mathbf{u},\Theta). \tag{3.13}$$

Here $\Theta=(\mathbf{v},\mathbf{w},\mathbf{r})^T$ are the auxiliary variables, L_h, J_h are spatial discrete operators, and F_h is a semi-discrete auxiliary function enforcing the perfect matching.

We introduce the variable $\phi=\mathbf{u}_t$ to obtain a first order system in time, then take discrete Fourier transform in space. Temporal stability is determined by the eigenvalue problem

$$s\mathbf{U}=\widetilde{\mathbf{D}}_h\mathbf{U}. \tag{3.14}$$

Here

$$\tilde{\mathbf{D}}_h=\begin{pmatrix} \mathbf{0} & \mathbf{I} & \mathbf{0} & \mathbf{0} & \mathbf{0} \\ D_h+\eta\sigma_1\mathbf{I} & -\sigma_1\mathbf{I} & \frac{i\sigma_1}{\alpha_1 h}A_1\sin(hk_x) & \frac{i\sigma_1}{h}A_2\sin(hk_y) & -\eta\sigma_1\mathbf{I} \\ -\frac{i}{\alpha_1 h}\sin(hk_x)\mathbf{I} & \mathbf{0} & -(\eta+\sigma_1)\mathbf{I} & \mathbf{0} & \mathbf{0} \\ \frac{i}{h}\sin(hk_y)\mathbf{I} & \mathbf{0} & \mathbf{0} & -\eta\mathbf{I} & \mathbf{0} \\ \eta\mathbf{I} & \mathbf{0} & \mathbf{0} & \mathbf{0} & -\eta\mathbf{I} \end{pmatrix},$$

and

$$D_h=-\frac{4}{(\alpha_1 h)^2}A_1\sin^2\Big(\frac{hk_x}{2}\Big)-\frac{4}{h^2}A_2\sin^2\Big(\frac{hk_y}{2}\Big)-\frac{1}{\alpha_1 h^2}A_3\sin(hk_x)\sin(hk_y),$$

is the (discrete) Fourier transform of the discrete approximations of the right-hand side of (2.3). If $\sin(k_x h)/h\approx k_x$ and $\sin(k_y h)/h\approx k_y$ we say that the corresponding mode is well-resolved. Otherwise it is un-resolved. In a discrete setting the behavior of un-resolved modes may differ significantly from what continuous analysis predicts.

To investigate the stability of a numerical approximation at a certain resolution we can compute the eigenvalues of $\widetilde{\mathbf{D}}_h$ for all wave numbers represented on the grid. In

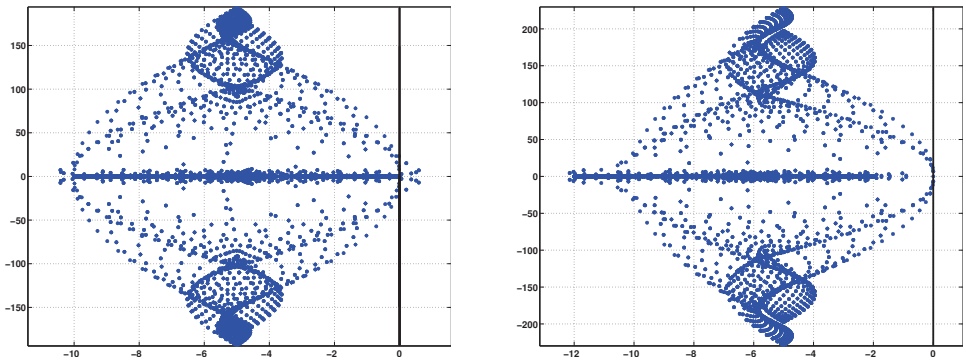

(a) MA2 (Apatite) $\eta=0$, $\alpha_1=1$, $\sigma_1=10$.

(b) MA2 (Apatite) $\eta=2$, $\alpha_1=0.8$, $\sigma_1=10$.

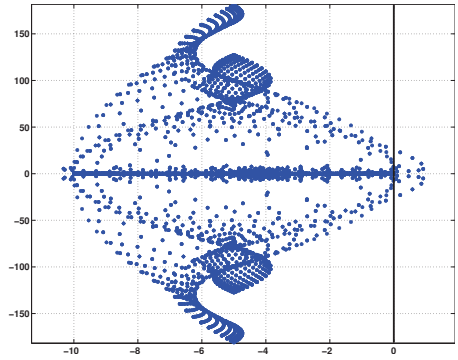

(c) MA4 (Zinc crystal) $\eta=0$, $\alpha_1=1$, $\sigma_1=10$.

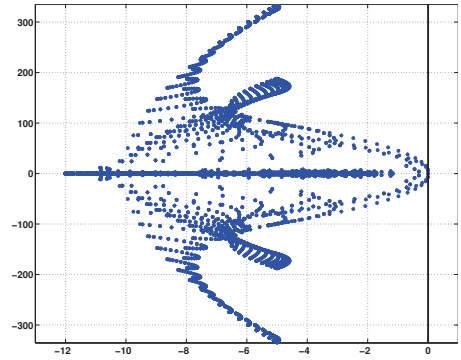

(d) MA4 (Zinc crystal) $\eta=2$, $\alpha_1=0.5$, $\sigma_1=10$.

Figure 3: The discrete spectrum of the vertical layer (parallel to the y-axis) for Materials MA2 (Apatite) and MA4 (Zinc crystal).

Fig. 3, we have plotted the eigenvalues for Apatite and Zinc crystal when $h=0.05$. In Figs. 3(a) and 3(c) there is no grid compression. In both cases there are only a few unstable eigenmodes, with $k_1\sim h$ and $k_2\sim 1$. These unstable modes are well resolved and have frequencies corresponding to the unstable part of the slowness curve. There are other discrete modes, with higher frequencies (not well resolved), also corresponding to the unstable part of the slowness curve, but these are in fact stable. This indicates that the semi-discrete PML (3.13) has significantly more robust stability properties than the corresponding continuous PML (2.13). In Paper II of [26], the stability of a simpler system, discretized in second order form, is analyzed in detail. The result supports the claim.

The well-resolved modes behave as predicted by the continuous analysis, and by Lemma 4 can be stabilized by the grid compression parameter α_1. This is illustrated, as seen in Figs. 3(b) and 3(d), where we also used a complex frequency shift to stabilize the non-physical modes. However, as we refine the mesh, more unstable, well resolved physical modes appear. These unstable modes can also be stabilized by reducing α_1 further. Asymptotically we expect to use $\alpha_1\sim h$.

3.4 Stability of the corner region

If a Cartesian grid is surrounded by perfectly matched layers, corner regions are introduced where both damping coefficients are non-zero, $\sigma_1, \sigma_2 > 0$. In order to understand the behavior of the entire scheme, it is useful to investigate the stability of this corner region. In this section we show that the full PML formulation (2.12) is significantly more stable. We know that in the continuous setting at sufficiently high frequencies the complex frequency shift η stabilizes the non-physical modes but does not guarantee the stability of the physical modes. We therefore consider the standard PML with $\eta=0$, $\alpha_1=\alpha_2=1$, (3.15) and investigate the stability of the physical modes in the corner region

$$\mathbf{u}_{tt} = A_1\mathbf{u}_{xx} + A_2\mathbf{u}_{yy} + A_3\mathbf{u}_{xy} - A_1(\sigma_1\mathbf{v} - \sigma_2\mathbf{w})_x + A_2(\sigma_1\mathbf{q} - \sigma_2\mathbf{p})_y - (\sigma_1+\sigma_2)\mathbf{u}_t - \sigma_1\sigma_2\mathbf{u}, \tag{3.15a}$$

$$\mathbf{v}_t = \mathbf{u}_x + \sigma_2\mathbf{w} - \sigma_1\mathbf{v}, \quad \mathbf{w}_t = \mathbf{u}_x, \quad \mathbf{p}_t = \mathbf{u}_y + \sigma_1\mathbf{q} - \sigma_2\mathbf{p}, \quad \mathbf{q}_t = \mathbf{u}_y. \tag{3.15b}$$

We will prove the following Lemma.

Lemma 3.5. *Consider the constant coefficient PML* (3.15) *with* $\sigma_1 = \sigma_2 = \sigma > 0$. *The physical modes are stable for all frequencies.*

Proof. For $\sigma_1=\sigma_2=\sigma\geq 0$, the auxiliary variables can be excluded. The roots corresponding to the physical modes satisfy the dispersion relation

$$F_0(s+\sigma, k_x, k_y) = 0.$$

Thus, any $\sigma > 0$ moves the physical modes into the left half plane and the PML is stable. So, the lemma is proved. □

A perturbation argument can be used to show that as long as σ_1 and σ_2 are sufficiently close the PML is stable. Computations of the corresponding spectrum as in Section 3.3 shows that the constant coefficients PML (3.15) is stable for all combinations of $\sigma_1 > 0$, $\sigma_2 > 0$. Therefore, we expect the corner region to always enhance the stability of the PML.

4 Numerical experiments

In this section, we present some numerical experiments. The experiments aim at validating the theoretical results and further exploring the efficiency and stability properties of the proposed layers. Firstly, we shall briefly present the numerical method used. We will then discuss each problem set up, describe the numerical experiments, and finally present and discuss numerical results.

4.1 Numerical method

The numerical scheme is a node centered second order accurate (both in time and space) finite difference scheme. We will start with the spatial discretization and the time stepping scheme will follow.

4.1.1 Spatial discretization

Let the grid in (x,y) coordinates be defined by

$$x_i = ih_x, \qquad i=0,\cdots,N_x-1, \qquad h_x=\frac{1}{(N_x-1)},$$
$$y_j = jh_y, \qquad j=0,\cdots,N_y-1, \qquad h_y=\frac{1}{(N_y-1)}.$$

We denote the grid function by $[\mathbf{u}_{i,j}]$. The standard finite difference operators are defined by

$$h_xD_+^x\mathbf{u}_{i,j}=\mathbf{u}_{i,j+1}-\mathbf{u}_{i,j}, \quad h_yD_+^y\mathbf{u}_{i,j}=u_{i+1,j}-\mathbf{u}_{i,j}, \quad h_xD_-^x\mathbf{u}_{i,j}=\mathbf{u}_{i,j}-\mathbf{u}_{i,j-1},$$
$$h_yD_-^y\mathbf{u}_{i,j}=\mathbf{u}_{i,j}-\mathbf{u}_{i-1,j}, \quad 2D_0^x\mathbf{u}_{i,j}=D_+^x\mathbf{u}_{i,j}+D_-^x\mathbf{u}_{i,j}, \quad 2D_0^y\mathbf{u}_{i,j}=D_+^y\mathbf{u}_{i,j}+D_-^y\mathbf{u}_{i,j}.$$

We also used averaging operators

$$2E_{\frac{1}{2}}^x(\sigma_{i,j})=\sigma_{i,j+1}+\sigma_{i,j}, \qquad 2E_{\frac{1}{2}}^y(\sigma_{i,j})=\sigma_{i+1,j}+\sigma_{i,j}.$$

Replacing spatial derivatives with differences in (2.12) yields the semi-discrete problem

$$\mathbf{u}_{tt}+(\sigma_1+\sigma_2)\mathbf{u}_t=L_h(\mathbf{u})+F_h(\mathbf{u},\Theta,\sigma_1,\sigma_2,\eta), \qquad \Theta_t=J_h(\mathbf{u},\Theta). \tag{4.1}$$

Here $\Theta=[\mathbf{v},\mathbf{w},\mathbf{p},\mathbf{q},\mathbf{r},\mathbf{z}]^T$, are the auxiliary variables and L_h,J_h are spatial discrete operators. The auxiliary function $F_h(\mathbf{u},\Theta,\sigma_1,\sigma_2,\eta)$ ensures the perfect matching.

4.1.2 Temporal discretization

We introduce the discrete time variable, $t_n=ndt$, $n\in\mathbb{N}$, where dt is the time step and $\mathbf{u}^n\approx\mathbf{u}(t_n)$. The usual finite difference operators with respect to time are denoted by

$$dt^2D^{tt}\mathbf{u}^n=\mathbf{u}^{n+1}-2\mathbf{u}^n+\mathbf{u}^{n-1}, \qquad 2dtD_0^t\mathbf{u}^n=\mathbf{u}^{n+1}-\mathbf{u}^{n-1}, \quad dtD_+^t\mathbf{u}^n=\mathbf{u}^{n+1}-\mathbf{u}^n.$$

The time integration scheme uses, the leap-frog scheme for the physical variable and the Crank-Nicolson scheme for the auxiliary variables. The fully discrete PML problem is

$$D^{tt}\mathbf{u}^n+(\sigma_1+\sigma_2)D_0^t\mathbf{u}^n=L_h(\mathbf{u}^n)+F_h(\mathbf{u}^n,\Theta^n,\sigma_1,\sigma_2,\eta), \tag{4.2a}$$
$$D_+^t\Theta^n=\frac{1}{2}J_h(\mathbf{u}^{n+1},\Theta^{n+1})+\frac{1}{2}J_h(\mathbf{u}^n,\Theta^n). \tag{4.2b}$$

The discrete problem

$$D^{tt}\mathbf{u}^n=L_h(\mathbf{u}^n), \tag{4.3}$$

corresponds to the interior discretization of the elastic wave equation (2.3), can be shown to conserve discrete energy, see [13].

4.2 Stability of the PML

The aim of this subsection is to numerically study the dynamic behavior of the discrete PML model. We are particularly interested on how growth depends on the complex frequency shift η, the magnitude and variability of the damping parameter, the mesh size and the material parameters. We consider a square $(x,y)\in[-1,1]\times[-1,1]$ with damping everywhere. To mimic a vertical layer we use $\sigma_1(x)=5(n+1)|x|^n$, $\sigma_2(y)=0$, while a horizontal layer is obtained by $\sigma_1(x)=0$, $\sigma_2(y)=5(n+1)|y|^n$. Here n is a non-negative integer. We use $\eta=1+0.1\sigma_1$ such that the conditions in Lemma 3.2 are satisfied. In all forthcoming experiments in this section we set $\alpha_1=1$, $\alpha_2=1$ and consider the initial data

$$u_1=u_2=\exp\Big(-\ln(2)\frac{x^2+y^2}{\delta}\Big),\qquad \delta=0.02, \tag{4.4a}$$

$$u_{1t}=u_{2t}=0, \tag{4.4b}$$

for the displacement field and homogeneous initial data for the auxiliary variables.

We begin with the strongly unstable material MA1 on a uniform grid, with $h_x=h_y=0.05$, (that is there are about 15 points in the initial pulse) and study the behavior of the vertical layer by setting $\sigma_2=0$. Homogeneous Dirichlet boundary conditions are imposed in the x-direction and the boundaries in the y-direction are closed with periodic boundary conditions. We run the simulations until time $T=50$, for $n=\{0,2,4,6,8\}$. Numerical results are displayed in Fig. 4(a) for $\eta=0$ and in Fig. 4(b) for $\eta=1+0.1\sigma_1$.

As predicted by the analysis in the preceding section, at constant coefficients the PML solutions grow in time and growth depends on $\max\sigma_1$, see Figs. 4(a), 4(b) and also Fig. 4(d). Growth also remains for variable coefficients. With our choice of damping function the local values of σ_1 decreases with increasing degree of the monomial in a large part of the layer, and therefore it is not surprising that the growth rate decreases with increasing monomial degree, see also Figs. 4(a) and 4(b). However, with grid refinement this behavior will probably change. In conclusion, for a given resolution, using higher order monomials seems advantageous as the damping power of the layer can be held constant by our choice of damping function while reducing the severity of the growth.

Theoretical analysis at constant coefficients also predicts that the complex frequency shift stabilizes the non-physical modes. We see from Figs. 4(a) and 4(b), the introduction of the complex frequency shift reduces the growth rate significantly. However, the absorption power of the PML for a fixed width layer is weakened.

Next we fix the PML parameters and vary the mesh-size $h_x=h_y=\{0.2,0.1,0.05,0.025\}$. From Fig. 4(c), we see that the growth rate increases with resolution, but the growth rate approaches a constant-the theoretical growth rate-as we refine the mesh. These results complement the semi-discrete analysis in the last section and support the conclusion that only well-resolved modes corresponding to the unstable part of the slowness curve are unstable.

In the last sets of the experiment, the mesh-size is $h_x=h_y=0.05$, the PML parameters are held constant, and we vary the material parameters. Here we study the behavior of

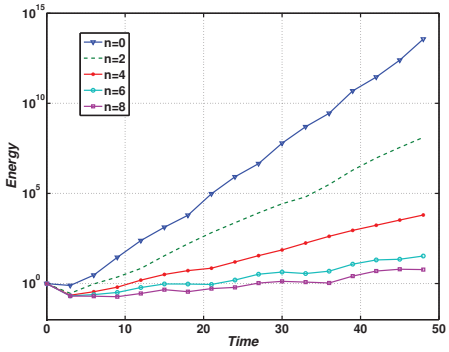

(a) Vertical layer $\eta=0$.

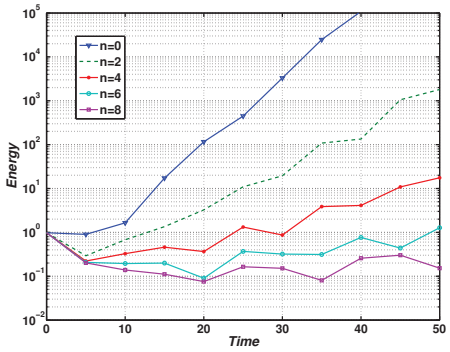

(b) Vertical layer $\eta=1+0.1\sigma_1$.

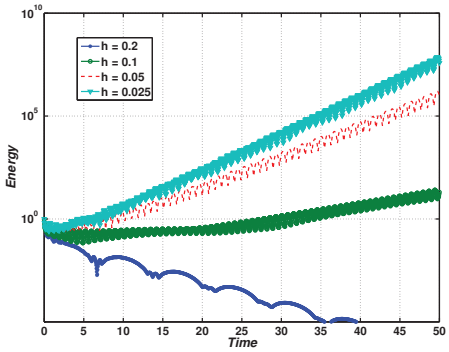

(c) Vertical layer $\eta=1+0.1\sigma_1$, $\sigma_1=5$.

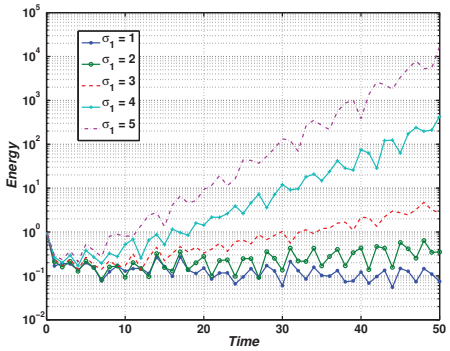

(d) Vertical layer $\eta=1+0.1\sigma_1$, $\sigma_1=const.$

Figure 4: The maximum elastic energy ($\|\sqrt{u_1^2+u_2^2}\|_\infty$).

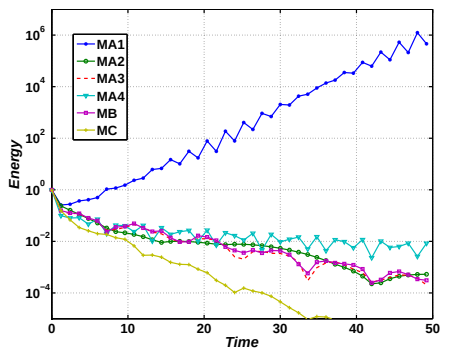

(a) Vertical layer $\eta=1$, $\sigma_1=5$.

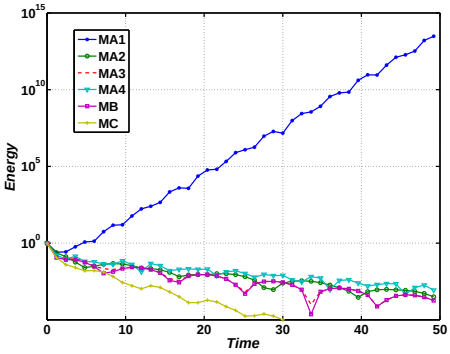

(b) Horizontal layer $\eta=1$, $\sigma_1=5$.

Figure 5: The maximum elastic energy ($\|\sqrt{u_1^2+u_2^2}\|_\infty$), $h=0.05$.

both the vertical layer and the horizontal layer. In Fig. 5, we see that growth rate depends also on the material parameters, that is the degree of violation of the geometric stability condition. From the slowness diagrams for material MA1 we know that the geometric

stability condition is more severely violated in the y-direction than in the x-direction, therefore it is not surprising that the growth rate for the horizontal layer is larger than that of the vertical layer. We note that if the violation of the geometric stability is mild (as in MA2, MA3, MA4), on a reasonably fine mesh the discrete PML is be stable, see Fig. 5.

4.3 Ducted problem

In this subsection we apply the PML to a ducted elastic wave problem. The physical domain is the infinite strip $-5\leq x\leq 5$, $-\infty<y<\infty$. The problem is periodic in the x-direction, but extends to the infinite space in the y-direction. In order to perform numerical experiments we truncate the domain in the y-direction such that the computational domain is a square $-5\leq x\leq 5$, $-5\leq y\leq 5$. To simulate the infinite space, we add two additional layers, $5\leq|y|\leq 6$ (see Fig. 6) in which the PML equations are solved. For the displacement field we use the initial data

$$u_1=u_2=\exp\Big(-\ln(2)\frac{x^2+y^2}{\delta}\Big),\qquad \delta=0.2, \tag{4.5a}$$

$$u_{1t}=u_{2t}=0. \tag{4.5b}$$

Homogeneous initial data are used for the auxiliary variables. We set homogeneous Dirichlet boundary conditions in the y-direction, and periodic boundary conditions in the x-direction.

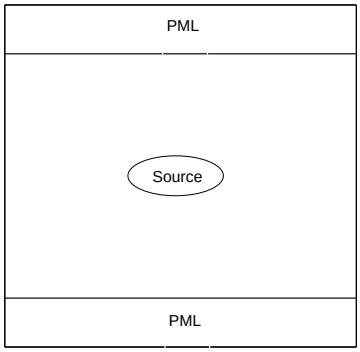

Figure 6: Computational domain.

The damping profile is the monomial of the form

$$\sigma_2(y)=\begin{cases} 0, & \text{if } |y|\leq y_0,\\ d_0\Big(\frac{|y|-y_0}{y_1-y_0}\Big)^n, & \text{if } |y|\geq y_0,\end{cases}$$

$$d_0>0,\quad n=4,\quad y_0=5,\quad y_1=6.$$

The velocities of the P-wave and S-wave are denoted C_p, C_s. We choose $d_0=C_p(n+1)/(2(y_1-y_0))\log(1/Ref)$ such that the relative error from the outer boundaries is of the

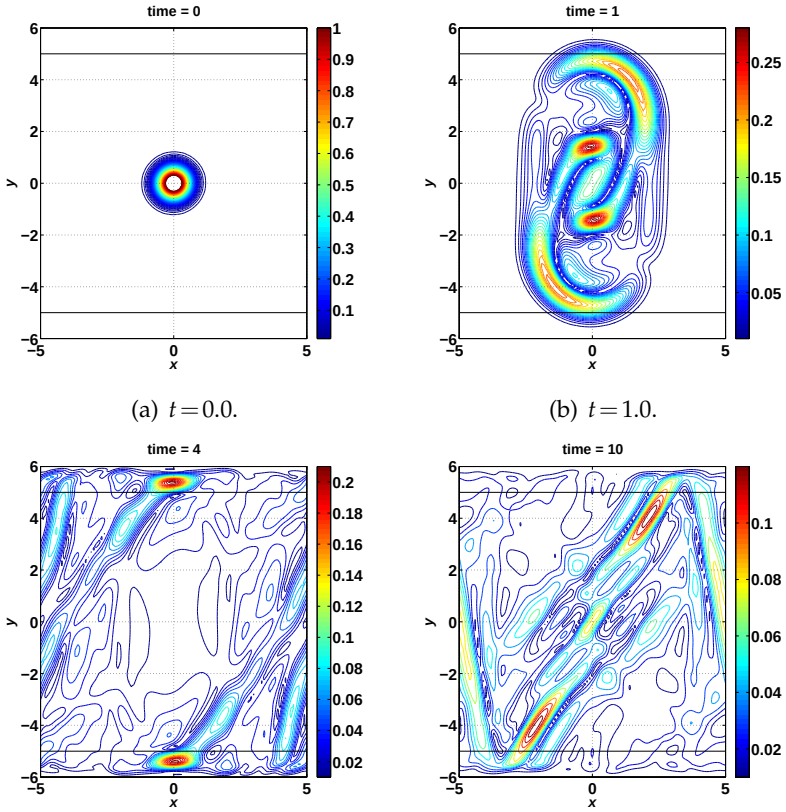

(a) $t=0.0$. (b) $t=1.0$.

(c) $t=4.0$. (d) $t=10.0$.

Figure 7: The dynamics of $\sqrt{u_1^2+u_2^2}$ for the new second order PML for the "unstable" Material MA1. All figures are with contours between 0 and 1 at intervals of 0.01, exempting the zero contour. Note that the color code changes, red and blue colors correspond to the maximum energy and minimum energy respectively in the interval $[0.01,1]$.

magnitude *Ref*, see [4, 23]. Here, $C_p=4.5$ is the maximum wave speed for the elastic materials considered. Note that if d_0 is large it may cause stiffness.

In order to highlight the effectiveness of the proposed layers we consider the difficult elastic material MA1 (and the strongly "unstable" horizontal layer).

We discretize the domain by introducing the uniform mesh-size $h_x=h_y=0.1$ such that the initial pulse is well resolved. We set the relative error of magnitude $Ref=10^{-3}$, introduced the complex frequency shift $\eta=1+0.1\sigma_2$ and compute the solutions until $T=70$. The behavior of the PML is illustrated in Fig. 7, showing how the initial pulse spreads, enters into the layer and is being absorbed. After a long time, $T=70$, the growing solutions corrupts the solution in the interior of the domain, see Fig. 8(a). To study the dependence of growth on the mesh-size, we coarsened the mesh $h_x=h_y=0.2$ and compute until $T=70$, and there was no growth, see Fig. 8(b). However, if the computation is

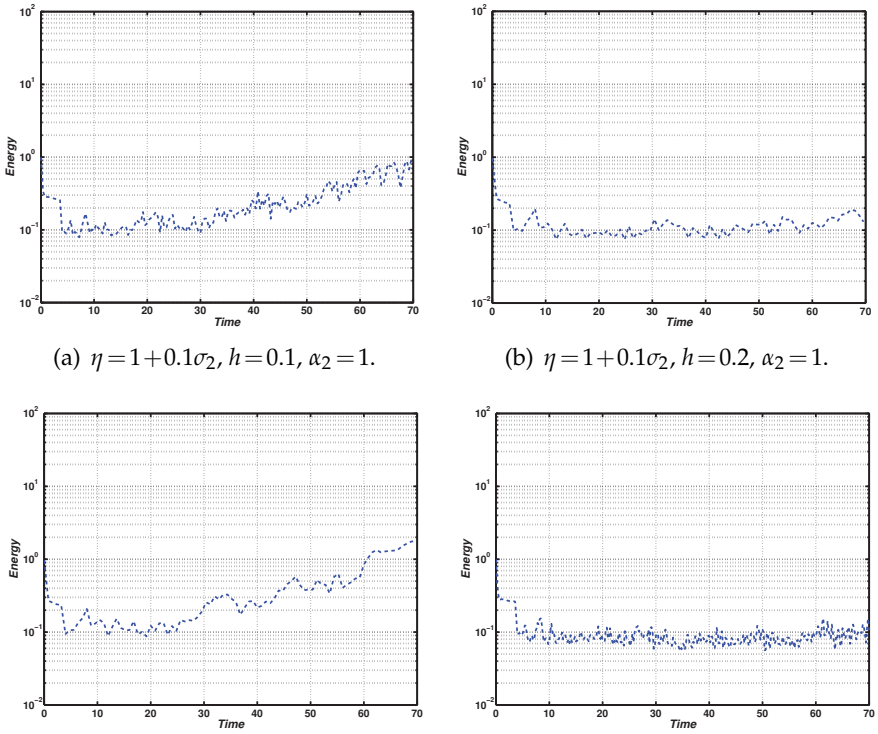

(a) $\eta=1+0.1\sigma_2$, $h=0.1$, $\alpha_2=1$.

(b) $\eta=1+0.1\sigma_2$, $h=0.2$, $\alpha_2=1$.

(c) $\eta=0.0$, $h=0.2$, $\alpha_2=1$.

(d) $\eta=1+0.1\sigma_2$, $h=0.1$, $\alpha_2=1-0.5\exp(-1/(5(|y|-5))$.

Figure 8: The maximum energy $\|\sqrt{u_1^2+u_2^2}\|_\infty$ in the interior of the domain.

extended to $T=100$ we see a slow growth in energy. Next, we set the complex frequency shift $\eta=0$ the growing solutions reappear, see Fig. 8(c), highlighting the stabilizing effect of the complex frequency shift.

Numerical experiments were also performed for the materials MA2, MA3, and MA4. For these materials and at the above refinement levels, no growth was seen in the layer, even at late times. This behavior would probably change with further refinements. The explanation is that if the violation of the geometric stability condition is mild, on a reasonably fine mesh the discrete PML is stable.

In order to further investigate the behavior of the layer we repeat the above experiment for material MA1 (with $\eta=0$, $h=0.1$) and zoom very close to the layer $((x,y)\in[-5,5]\times[5,6])$ as shown in Fig. 9. We carefully study the dynamics of the waves transmitted into the layer. Observe that the solutions in the layer are smooth and waves propagating normal to the boundary are perfectly absorbed. The remnant propagates tangentially unabsorbed in the layer. Because of the periodic boundary conditions in the tangential direction, with increasing time waves propagate back and forth in the layer and grow slowly, see Fig. 9.

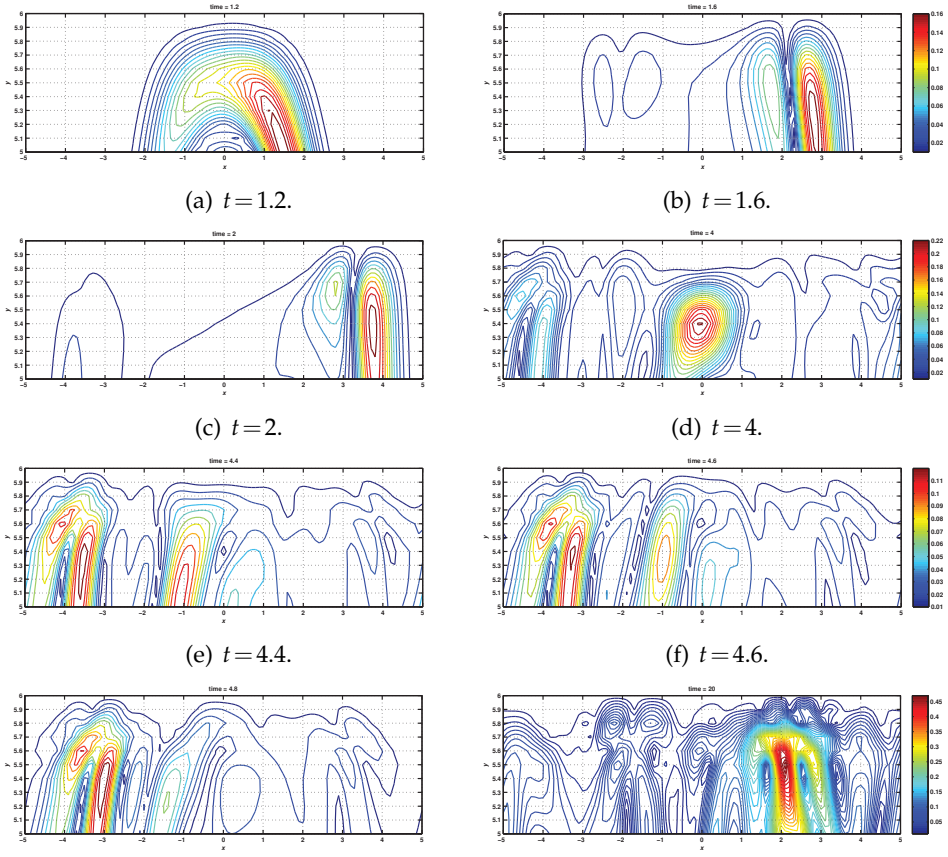

(a) $t=1.2$. (b) $t=1.6$.

(c) $t=2$. (d) $t=4$.

(e) $t=4.4$. (f) $t=4.6$.

(g) $t=4.8$. (h) $t=20$.

Figure 9: The dynamics of $\sqrt{u_1^2+u_2^2}$ inside the PML for the "unstable" Material MA1. All figures are with contours between 0 and 1 at intervals of 0.01, exempting the zero contour. Note that the color code changes, red and blue colors correspond to the maximum energy and minimum energy respectively in the interval $[0.01,1]$.

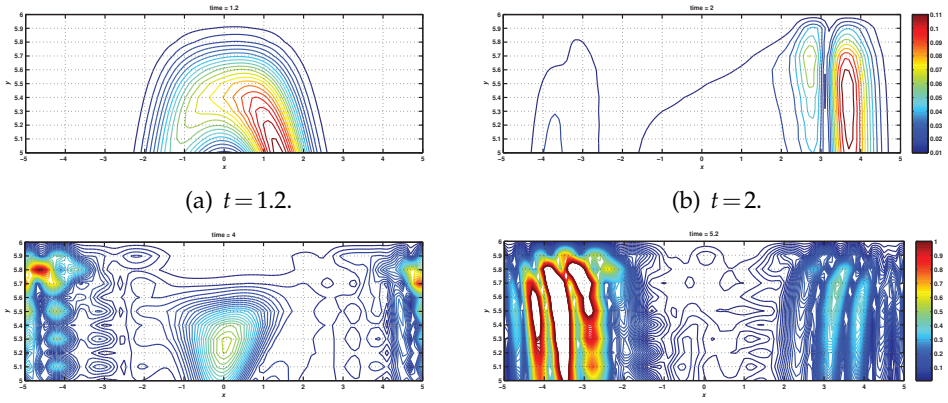

(a) $t=1.2$. (b) $t=2$.

(c) $t=4$. (d) $t=5.2$.

Figure 10: Same as Fig. 9, except for dynamics inside the split-field PML.

In order to make a comparison we apply the split-field PML [4, 23] to the first order (velocity-stress) formulation of the elastic wave equation. Considering the same set-up and resolution $h=0.1$ as above, we discretized the equations using standard second order accurate centered finite difference approximations in space and standard second order Runge-Kutta method in time. We compute the solutions until a final time T. Since we are interested in the behavior of the layer we zoom very close to the layer $((x,y)\in[-5,5]\times[5,6])$ as shown in Fig. 10. We see that as the slower S-wave penetrates the layer, at approximately $t=4.0$ the solution in the layer in this case grows destructively in time. As before, the mesh was coarsened and the solutions remained unstable but with a slower growth rate. We believe the strong instability observed here and reported in [4, 5] is related to the high-frequency parasitic numerical modes that are present in the standard discretization of the first order formulation. Analysis of the discrete behavior of PML models is a topic of Paper II in [26], where the stability of a simpler system, discretized in second order form is analyzed in detail.

4.3.1 Grid compression

From the analysis, we expect that for a given resolution, the introduction of a grid compression parameter will stabilize the physical modes. This idea was tested for material MA1 and the resolution $h_x=h_y=0.1$, for that case we observed growth, see Fig. 8(a). A grid compression $\alpha_2=1-0.5\exp(-1/(5(|y|-5))$ was introduced in the layer and it resulted to a stable solution, see Fig. 8(d). However, as we refine the grid we expect the growth to reappear. That growth can also be removed by further reducing the size of α_2. A von-Neumann analysis yields the CFL condition

$$dt<\Big(\frac{2\alpha_2^2}{1+\alpha_2^2}\Big)^{\frac{1}{2}}\Big(\frac{1}{C_p^2+C_s^2}\Big)^{\frac{1}{2}}h. \tag{4.6}$$

Note that if $\alpha_2=1$, we recover the CFL condition derived in [13]. The drawback here is that the problem becomes increasingly stiff with decreasing α_2, which consequently will restrict the time step. Let W_0 denote the work required when $\alpha_2=1$. If $\alpha_2<1$, work scales $\sim 1/\alpha_2 W_0$. From the analysis, we expect to use $\alpha_2\sim h$, asymptotically. Therefore work scales $\sim N_y W_0$.

4.4 Open domain

We consider an open domain problem. The computational domain is the rectangular two-dimensional domain $(x,y)\in[-10,10]\times[-10,10]$, completely surrounded by a PML of width 2. The damping profile is a 4th degree monomial $n=4$. We chose the damping coefficient d_0 so that we a relative error of magnitude $Ref=2\times10^{-2}$. The complex frequency shift is $\eta=1.0$. If a Cartesian grid is surrounded by the PML, $\eta=1$, independent of damping is sufficient for stability. No artificial dissipation or grid compression was

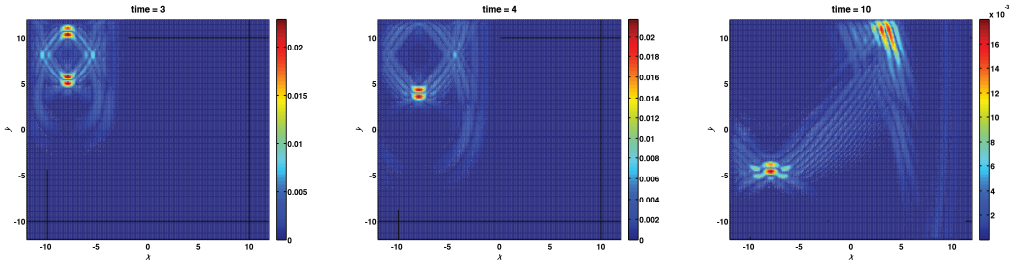

(a) $t=3$. (b) $t=4$. (c) $t=10$.

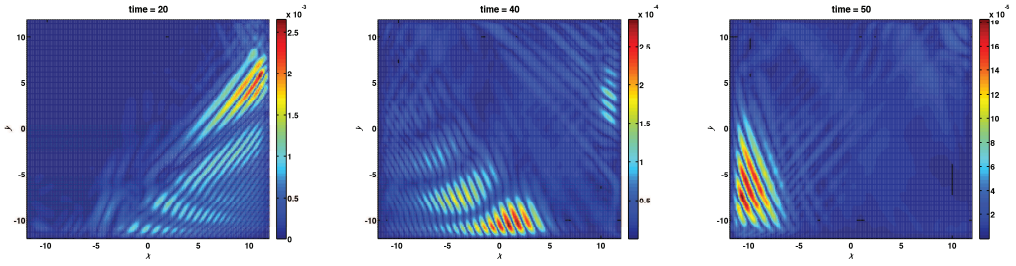

(d) $t=20$. (e) $t=40$. (f) $t=50$.

Figure 11: The dynamics of $\sqrt{u_1^2+u_2^2}$ for MA1, with $h=0.125$, $n=4$. Note that the color code changes, red corresponds to the maximum energy on the grid and the blue color is the minimum energy on the grid.

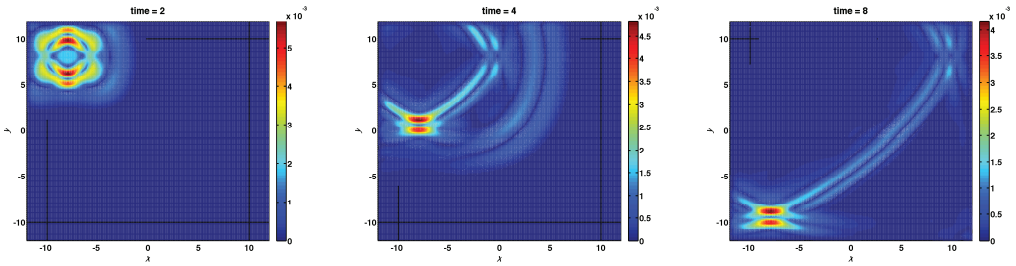

(a) $t=2$. (b) $t=4$. (c) $t=8$.

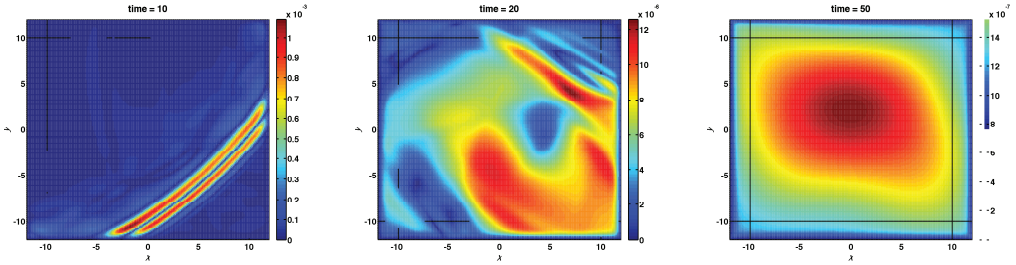

(d) $t=10$. (e) $t=20$. (f) $t=50$.

Figure 12: Same as Fig. 11, except for MA2.

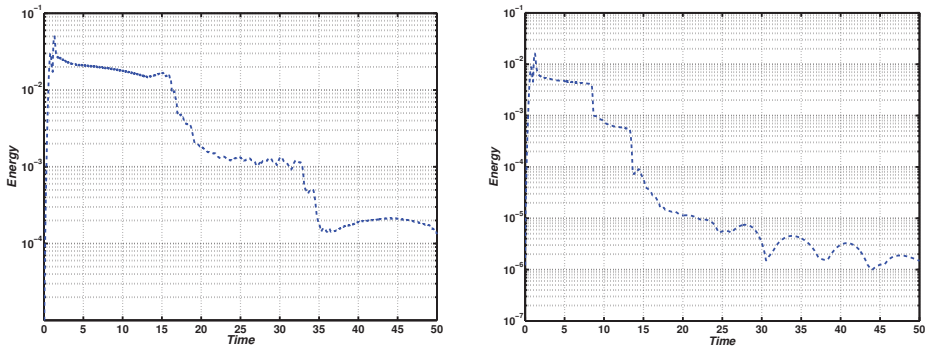

(a) MA1. (b) MA2.

Figure 13: The maximum elastic energy ($\|\sqrt{u_1^2+u_2^2}\|_\infty$) inside the computational domain, with $h=0.125$, $n=4$.

used, that is $\alpha_1=\alpha_2=1$. We force the first component of the displacement vector with

$$F(x,y,t)=f(t)\frac{1}{\delta}e^{-\frac{7((x-8)^2+(y+8)^2)}{\delta}},$$
$$f(t)=(2\pi^2(0.9t-1)^2-1)e^{-\pi(0.9t-1)^2}, \qquad \delta=0.025.$$

An equidistant grid with $h_x=h_y=0.125$ is used everywhere. This means that there are about 10 points across the pulse in the source term. We compute the solution until $T=50.0$. The behavior of the model is displayed in Fig. 11 for material MA1 and in Fig. 12 for material MA2, showing how the wave generated by the source field $F(x,y,t)$ spreads, penetrates the PML and it is being absorbed. Fig. 13, shows the time history of the maximum energy $\|\sqrt{u_1^2+u_2^2}\|_\infty$ in the interior of the computational domain, showing the stability of the layer and long time decay of the energy.

For material MA1, we first observed a slowly growing solution in the layer ($(x,y)\in[-12,12]\times[10,12]$). Later the growing solution enters the corner region ($(x,y)\in[10,12]\times[10,12]$) and decays in time, (note the changing exponent in Fig. 11). Furthermore, if we set the damping to a 6th degree monomial (for $h=0.125$) or coarsen the mesh $h=0.2$ (for the 4th degree monomial), we did not observe any growth in the layers. For the material MA2 there was no growth observed with these resolutions, but with further refinement we may expect to see some intermediate growth also for material MA2.

4.5 Convergence

From application point of view, convergence is the ability of a numerical procedure to yield arbitrarily small errors at the expense of work. Often errors can be made to depend on one parameter, the mesh-size h. When a PML model is used in a numerical computation, errors can be divided into 3 different categories: the discretization error, numerical reflection, and the modeling error. The discretization error is the generic error that comes

with any numerical method (for example by approximating derivatives by differences). The numerical reflections are the spurious discrete effects introduced by discretizing the PML and seen in the interior domain. The modeling error is introduced because the layer has a finite width. The discretization error and numerical reflection should vanish as the mesh-size approaches zero and the modeling error decreases as the magnitude of damping coefficient or the PML width increases.

Here we show that we can choose the PML parameters (for a fixed PML width) as a function of the grid-size h such that the total PML error (modeling error + numerical reflection) converges to zero as we refine the mesh. In the forthcoming experiments we consider the "strongly unstable" material MA1 in the domain

$$\Omega=\{-2\leq x\leq 2,\ \ 2\leq y\leq 2\}. \tag{4.7}$$

The initial data is given by (4.5) with $\delta=0.05$. In order to avoid unnecessary stiffness we chose the damping profile as a monomial of degree $n=3$. We set

$$d_0=(n+1)\times\frac{4.5}{(\alpha\times d)}\times\log\Big(\frac{1}{(C_0h^2)}\Big). \tag{4.8}$$

The factor α is included to compensate for the fact that the grid compression modifies the wave speed. $C_0=0.01$ has been empirically determined and d is the width of the PML. In this case the numerical scheme in the interior converges quadratically. Therefore, the discretization error approaches zero at the rate $\mathcal{O}(h^2)$, the modeling error converges at the rate

$$\exp(-\int\sigma d\xi)=C_0h^2$$

and the numerical reflection should converge at the rate $\mathcal{O}(d_0h^2)=\mathcal{O}(h^2|\log(h)|)$, if $\alpha=1$. However if $\alpha\sim h$ the convergence rate of numerical reflections reduces to $\mathcal{O}(h|\log(h)|)$. In both cases, the total PML error is expected to approach zero at the rate $\mathcal{O}(h^2|\log(h)|)$ if $\alpha=1$ and $\mathcal{O}(h|\log(h)|)$ if $\alpha\sim h$.

In the first experiment we surround the computational domain Ω with a PML of width $d=2$. No artificial dissipation, grid stretching or compression was used, that is $\alpha_1=\alpha_2=1$. The complex frequency shift is $\eta=0.1$. We compute the solution until $T=1.5$, so that the modeling error has a chance to affect the solution in the interior. We also compute a reference solution in a larger domain without the PML. By comparing the PML solution in the interior of the domain to the reference solution, measured in the L^2-norm and normalized by the L^2-norm of the initial data, we obtain an accurate measure of the relative PML error. In Fig. 14(a) we plot the time history of the PML error. The fast P-wave with velocity $C_p=4.5$ completely penetrates the layers at about $t=0.45$ and generates numerical reflection which level off before $t=1$. At about $t\approx 1$ the slow S-wave with velocity $C_s=2.3$ penetrates the layers while the modeling errors due to P-wave are simultaneously returning from the outer boundaries. At $t\geq 1$ the numerical reflection from the interface and the modeling error from the outer boundaries superimpose.

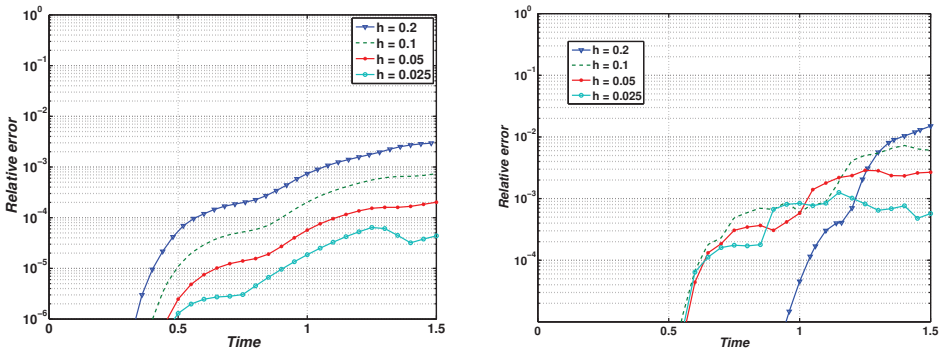

(a) Open domain. (b) Ducted domain.

Figure 14: Relative error as a function of time.

The effect on the solution in the interior levels off as time increases. However, from the choice of our damping coefficient, the convergence rate of the total PML error approaches $\mathcal{O}(h^2|\log(h)|)$, see Fig. 14(a) and columns 2 and 3 of Table 2.

Table 2: Relative error as a function of the mesh-size h.

	Open domain		Ducted domain	
mesh-size (h)	relative error	rate	relative error	rate
0.2000	2.1000×10^{-3}	–	1.1800×10^{-2}	–
0.1000	5.4612×10^{-4}	1.9499	5.0000×10^{-3}	1.2211
0.0500	1.4988×10^{-4}	1.8654	2.6000×10^{-3}	0.9478
0.0250	4.3763×10^{-5}	1.7760	5.7161×10^{-4}	2.1930

We note that no growth was seen even at late times. The remnant of the wave not damped in the layer where $\sigma_1 = 0$ or $\sigma_2 = 0$, propagates immediately into the corner region and decays exponentially in time. It is pertinent to note that if a Cartesian grid is surrounded by the PML no grid compression (or grid stretching) is needed to guarantee stability. The PML closure itself is asymptotically stable for all material parameters. We also recover the CFL condition of the interior scheme.

Next, we consider the case where the PML is placed only in one direction, and in the tangential directions the computational boundaries are terminated with periodic boundary conditions. The absence of the stabilizing corner regions can make convergence a difficult problem if we consider elastic materials violating the geometric stability conditions. The problem is made more difficult as we consider material MA1 and the strongly unstable horizontal layer.

In the previous section we showed that the grid compression parameter can be used to stabilize a discrete PML. Here we use the idea to achieve a stable PML for a fixed width layer with errors converging to zero as the grid is refined. As before we consider the domain (4.7) and add a layer of width 2 only in the y-direction. Inside the layer we

introduce

$$\alpha_2(y) = 1-\beta\exp\Big(-\frac{1}{(5(|y|-2)}\Big),$$

such that

$$\alpha_2(y) \approx 1-\beta, \quad \text{for all } \ |y| \geq 3.$$

The layer comprises of a transition region $2 < |y| < 3$ and a damping region $3 \geq |y| \geq 4$. The damping $\sigma_2(y)$ is zero in the transition region and positive in the damping region. The damping coefficient is given by (4.8) with $\alpha = 1-\beta$ and $d = 2$. We use the following mesh-sizes and corresponding β values $h = 0.2, 0.1, 0.05, 0.025$, $\beta = 0, 0.25, 0.5, 0.75$.

For these values the discrete PML is stable. Note that for small values of h we have $\alpha \sim h$, which agrees with the results in Section 3.3. In this case the complex frequency shift is $\eta = 1+0.1\sigma_2$. As before we compute the solution until $T = 1.5$ and compare with a reference solution. See Fig. 14(b) for the time history of the PML error. The effect of the transition region is seen first, at $t \approx 0.6$ (except for the coarsest grid). This effect is reduced with refinement. The next increase in error is due to numerical reflections at the beginning of the damping region. Note that this effect is seen earlier for smaller h (and consequently smaller α) since the grid compression changes the wave speed. Effects of the modeling error is seen at the final time for all grids. With our choice of d_0 (4.8) we can at most expect the numerical reflections to converge towards zero at the rate $\mathcal{O}(d_0 h^2) = \mathcal{O}(h|\log(h)|)$, which will also be the expected rate for the total PML error. In Table 2 we have recorded errors for this case also. The table shows convergence, although somewhat erratic.

Remark 4.1. To avoid the deterioration of the convergence rate, one could use a layer of width $d \sim 1/\alpha$ and let the damping be independent of α. We would then expect to regain the convergence rate $\mathcal{O}(h^2|\log h|)$, but the growing layer would make the work increase faster with the number of points.

5 Conclusions

In this paper we derive a PML for the second order formulation of linear, anisotropic elastodynamics in two space dimensions. The layer equations are derived by applying a complex coordinate stretching directly to the second order equations. The resulting system is strongly hyperbolic. By a standard perturbation argument our PML at constant coefficients suffers from the same high frequency instability as the modal PML and the split field PML if the geometric stability condition is violated. We also find that the complex frequency shift has a stabilization effect. However, in computations using standard second order finite differences our PML behaves much better than a standard first order PML. We have found several reasons for this.

In a discrete setting modes corresponding to the unstable part of the slowness curve may not be represented or not well-resolved. In such cases the unstable temporal behavior predicted by the continuous analysis may not be valid. In fact, a straight forward

computations of the temporal eigenvalues corresponding to our discrete spatial operator in a constant coefficient setting shows that if unstable modes are not well resolved they are in fact stable. Computations using different resolutions verifies the conclusion also for the variable coefficient setting. We also show that this effect can be enhanced by coordinate compression in the layer. However, coordinate compression increases the stiffness of the problem.

Secondly, we observe that the geometric instability gives rise to growing modes, with bulk localized to part of the layer, and propagating tangentially. If a Cartesian domain is surrounded by layers, the bulk of the unstable mode eventually moves into a corner region, and decays. We analyze the stability properties of the corner region as before, finding that the corner region is significantly more stable.

Due to these types of behavior we have been able to construct discretely stable layers that yield reflections that converge to zero as the spatial step $h \to 0$, for a variety of anisotropic materials. The work required to compute a solution at a fixed time is $\sim Ch^{-3}$. When the domain is completely surrounded by PML the error due to the PML in the solution approaches zero at a rate corresponding to the theoretically predicted $\mathcal{O}(h^2|\log h|)$. In the difficult case of a ducted domain and a material that severely violates the geometric stability condition the PML error in our solution also approaches zero, but at best at the rate $\mathcal{O}(h|\log h|)$. The reduced convergence rate is related to the grid compression. Also note that the constant C in the work estimate may be large due to increased stiffness, which is again related to the grid compression.

References

[1] B. Sjogreen and N. A. Petersson, Perfectly matched layer for Maxwell's equations in second order formulation, J. Comput. Phys., 209 (2005), 19–46.

[2] H.-O. Kreiss, N. A. Petersson and J. Ystrom, Difference approximations for second order wave equation, SIAM J. Numer. Anal., 40 (2002), 1940–459.

[3] J. P. Berenger, A perfectly matched layer for the absorption of electromagnetic waves, J. Comput. Phys., 114 (1994), 185–200.

[4] E. Becache, S. Fauqueux and P. Joly, Stability of perfectly matched layers, group velocities and anisotropic waves, J. Comput. Phys., 188 (2003), 399–433.

[5] D. Appelo and G. Kreiss, A new absorbing layer for elastic waves, J. Comput. Phys., 215 (2006), 642–660.

[6] A. Taflove, Advances in Computational Electrodynamics, The Finite-Difference Time-Domain, Artec House Inc, 1998.

[7] J. Diaz and P. Joly, Stabilized perfectly matched layer for advective acoustics, Waves, (2003), 115–119.

[8] E. A. Skelton, S. D. M. Adams and R. V. Craster, Guided elastic waves and perfectly matched layers, Wave. Motion, 44 (2007), 573–592.

[9] S. Abarbanel, D. Gottlieb and J. S. Hesthaven, Long time behaviour of the perfectly matched layer equations in computational electromagnetics, J. Sci. Comput., 17(1-4) (2002), 405–422.

[10] D. Appelo and A. N. Petersson, A stable finite difference method for the elastic wave equation on complex domains with free surfaces, Commun. Comput. Phys., 5 (2009), 84–107.

[11] S. Abarbanel and D. Gottlieb, A mathematical analysis of the PML method, J. Comput. Phys., 134 (1997), 357–363.
[12] B. Gustafsson, H.-O. Kreiss and J. Oliger, Time Dependent Problems and Difference Methods, John Wileys and Sons, 1995.
[13] S. Nilsson, N. A. Petersson, B. Sjogreen and H.-O. Kreiss, Stable difference approximations for the elastic wave equation in second order formulation, SIAM J. Numer. Anal., 42 (2004), 1292–1323.
[14] M. Kuzuoglu and R. Mittra, Frequency dependence of the constitutive parameters of causal perfectly matched anisotropic absorbers, IEEE Microw. Guided. W., 6(12) (1996), 447–449.
[15] J. A. Roden and D. S. Gedney, Convolutional PML (CPML): an efficient fdtd implementation of the CFS-PML for arbitrary media, Microw. Opt. Tech. Lett., 27(5) (2000), 334–339.
[16] K. C. Meza-Fajardo and A. S. Papageogiou, A nonconvolutional, split-field, perfectly matched layer for wave propagation in isotropic and anisotropic elastic media: stability analysis, B. Seismol. Soc. Am., 98(4) (2008), 1811–1836.
[17] W. Chew and W. Weedon, A 3-D perfectly matched medium from modified Maxwell's equations with stretched coordinates, Micro. Opt. Tech. Lett., 7(13) (1994), 599–604.
[18] D. Komatitsch and J. Tromp, A perfectly matched layer absorbing boundary condition for the second order seismic wave equation, Geophys. J. Int., 154 (2003), 146–153.
[19] E. Becache, P. G. Petropoulos and S. D. Gedney, On the long-time behaviour of unplit perfectly matched layers, IEEE T. Antenn. Propag., 52(5) (2004), 1335–1342.
[20] P. Gallina, Effect of damping on assymetric systems, J. Vibrat. Acoust., 125 (2003), 359–365.
[21] D. Appelo and T. Colonius, A high-order super-grid absorbing layer and its application to linear hyperbolic systems, J. Comput. Phys., 228 (2009), 4200–4217.
[22] L. Thomsen, Weak elastic anisotropy, Geophysics, 51(10) (1986), 1954–1966.
[23] F. Collino and C. Tsogka, Application of the PML absorbing layer model to the linear elastodynamic problem in anisotropic heterogeneous media, Geophysics, 66 (2001), 294–307.
[24] T. Kato, Perturbation Theory for Linear Operators, Springer Verlag, 1966.
[25] W. M. Lai, D. Rubin and E. Krempl, Introduction to Continuum Mechanics, Butterworth-Heimann Ltd., US, 1993.
[26] K. Duru, Perfectly Matched Layer For Second Order Wave Equations, Licentiate Thesis, Div Sc. Comp., Dept. of Infor Tech., Uppsala University, ISSN 1404-5117; 2010-004, 2010.